Design and Characterization of W-Band SiGe RFICs for Passive Millimeter-Wave Imaging

Jason W. May, *Member, IEEE*, and Gabriel M. Rebeiz, *Fellow, IEEE*

***Abstract*—This paper describes the design and measurement of a wideband (W-band) passive radiometer chip developed in a standard 0.12-μm SiGe BiCMOS technology (IBM8HP, $f_t/f_{\max} = 200/265$ GHz). Design equations, simulations, and measurements are presented for a 94-GHz square-law detector and wideband low noise amplifier, and an 80–110-GHz single-pole double-throw switch. A total-power radiometer is presented, which can achieve a temperature resolution of $\approx$0.69 K (30-ms integration time) with periodic calibration or chopping above 10 kHz. A switched Dicke radiometer chip is also presented, which addresses the $1/f$ noise of the total-power radiometer, and can achieve a temperature resolution of 0.83 K with a 30-ms integration time. This performance is comparable to current III–V imaging modules, and demonstrates, to our knowledge, the first implementation of a SiGe or CMOS W-band radiometer on a single chip.**

***Index Terms*—Millimeter-wave detectors, millimeter-wave imaging, millimeter-wave integrated circuits (ICs), millimeter waves, passive imaging, radiometer.**

I. Introduction

MILLIMETER-WAVE imaging systems provide high spatial and temperature resolution while penetrating obscurants such as dust, fog, and clothing, thereby making them ideal for use in security scanners or collision avoidance systems. Active approaches include a transmitter that increases system complexity and cost, and experience image artifacts such as glint and speckle that require additional processing [1]. Passive systems, in contrast, collect the millimeter-wave radiation emitted by objects, but have reduced resolution at large distances [2]. Current wideband (W-band) passive imaging systems include high-responsivity zero-bias diodes [3], [4] in conjunction with GaAs or InP preamplifiers [5], [6], or fully passive diode arrays [7]. The zero-bias diode detection approach benefits from simplicity (no mixers), wide RF bandwidth, and reduced $1/f$ noise, but require a multichip solution. Discrete mixer-based passive imaging systems such as [8] and [9] may use Dicke switching to overcome $1/f$ noise, but suffer from a reduced detection bandwidth at the IF, increased size, and a much larger power consumption than passive systems. Recently, SiGe technologies with $f_t > 200$ GHz have made possible the development of fully integrated, highly compact, passive or active W-band (70–110 GHz) imaging systems [10].

In this paper, we present a W-band total-power radiometer and a W-band Dicke-switched radiometer using an on-chip detector circuit, low-noise amplifier (LNA), and single-pole double-throw (SPDT) switch in a commercial 0.12-μm SiGe process (IBM8HP, $f_t/f_{\max} = 200/265$ GHz). Section II reviews the total-power radiometer concept, the design and measurement of the W-band detector circuit, and presents a wideband 94-GHz LNA. Section III presents the Dicke radiometer topology together with the W-band SPDT S-parameters and complete radiometer results.

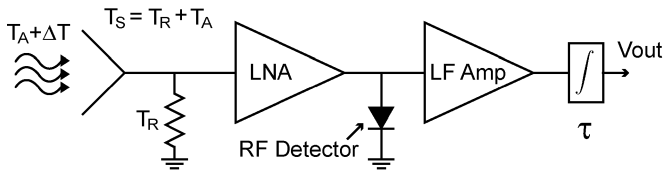

Fig. 1. Direct-detection total power radiometer. T_R is the LNA noise temperature, T_A is the average background temperature, and ΔT represents small variations in the scene temperature.

II. Total Power Radiometer SiGe Chip

A. System Topology

The proposed direct-detection total power radiometer is shown in Fig. 1, where T_S is the system noise temperature. The LNA and W-band detector are implemented in SiGe on a single chip followed by off-chip amplification and an integrator, and changes in the target temperature result to a dc change at the output. Millimeter-wave amplifiers, however, are known to exhibit low-frequency gain variations [11], and these LNA gain fluctuations are indistinguishable from a change in the target temperature. The minimum resolvable temperature for a total-power radiometer is given by

$$\Delta T_M = T_S \sqrt{\frac{1}{B\tau} + \left(\frac{\Delta G}{G}\right)^2} \tag{1}$$

where B is the RF bandwidth, τ is the integration time, T_S is the system noise temperature (see Fig. 1), and $\Delta G/G$ describes the LNA gain fluctuations [12]. ΔT_M is also commonly referred to as the noise-equivalent delta temperature (NEΔT or NEDT). Equation (1) neglects any additional noise generated by the detector circuit.

Manuscript received August 09, 2009; revised January 26, 2010. First published March 25, 2010; current version published May 12, 2010. This work was supported by the Defense Advanced Research Projects Agency Microantenna Arrays: Technology and Applications Program.

J. W. May was with the Electrical and Computer Engineering Department, University of California at San Diego, La Jolla, CA 92093 USA. He is now with HRL Laboratories LLC, Malibu, CA 90265 USA (e-mail: jwmay@hrl.com).

G. M. Rebeiz is with the Electrical and Computer Engineering Department, University of California at San Diego, La Jolla, CA 92093 USA (e-mail: rebeiz@ece.ucsd.edu).

Color versions of one or more of the figures in this paper are available online at http://ieeexplore.ieee.org.

Digital Object Identifier 10.1109/TMTT.2010.2042857

In a typical total-power radiometer imaging system, the effect of the LNA gain fluctuations can be removed by periodically aiming the receiver at a known reference temperature using a small mirror or mechanical scanning [13]. In this case, the minimum temperature resolution is given by the classic radiometer equation [14], as in (2). The LNA gain required is dependent upon the noise and responsivity of the detector, and is discussed in Section II-C

$$\Delta T_M = \frac{T_S}{\sqrt{B\tau}}. \tag{2}$$

Equation (2) shows that a large RF bandwidth improves the receiver temperature resolution, and several high-bandwidth SiGe/CMOS LNAs have been reported recently [15]–[18]. A sample calculation using an LNA noise figure of 8 dB, 20-GHz RF bandwidth, and 30-ms integration time (standard for video-rate imaging) yields $\Delta T_M = 0.075$ K. This is well below the 0.5-K threshold typically required to build a useful imaging system, indicating that it is possible to develop a W-band passive imager in SiGe if a low-noise square-law detector can be implemented on-chip.

B. W-Band Power Detector

The usual detector figure-of-merit is noise-equivalent power (NEP), and is given by the detector output rms noise voltage v_n divided by the responsivity $\Re$, i.e.,

$$\mathrm{NEP} = \frac{v_n}{\Re} = \frac{v_n}{\mathrm{V_{out\,dc}/Pin_{RF}}} \left(\frac{\mathrm{W}}{\sqrt{\mathrm{Hz}}}\right). \tag{3}$$

It is desirable to minimize NEP: for a standalone detector without preamplification, the detector NEP is related to ΔT_M by (4), where dv/dT is the change in output voltage per change in target temperature and k is the Boltzmann constant [5], [19]

$$\Delta T_M = \frac{v_n}{dv/dT} = \frac{\mathrm{NEP}}{kB\sqrt{2\tau}} \tag{4}$$

where a $\sqrt{2}$ is now present since the NEP is given in $\mathrm{V}/\sqrt{\mathrm{Hz}}$ (W/V), while (1) and (2) are based on noise temperature (or power), given in watts per hertz. For the case of a detector that is preceded by an LNA, the reader is referred to Section II-C.

Millimeter-wave Schottky diode detectors can be implemented in standard SiGe/CMOS processes [20], [21], but these typically have a high NEP in comparison to the high-responsivity III–V diodes presented in [3] and [4]. Although the III–V diodes are not compatible with SiGe/CMOS technology, a high-responsivity low-noise W-band SiGe detector circuit can be constructed, as shown in Fig. 2. The detector is a high-speed SiGe HBT biased in class B operation with a 94-GHz *LC* notch filter at the output port. The load resistance is chosen to be around 1 kΩ to obtain a high responsivity at video frequencies and to be noise matched to an external LNA (Stanford Research Systems, SRS 552). The notch filter suppresses the generation of unintended nonlinearities by reducing RF variations in V_{CE} and reduces the effect of transistor collector capacitances. The nonlinear HBT response can be analyzed using a large-signal model and assuming an ac ground at the collector [22]. As

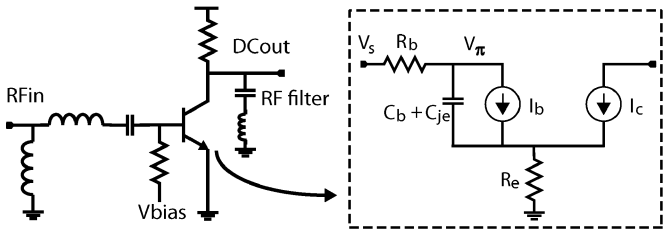

Fig. 2. Detector schematic and large-signal model for nonlinearity analysis.

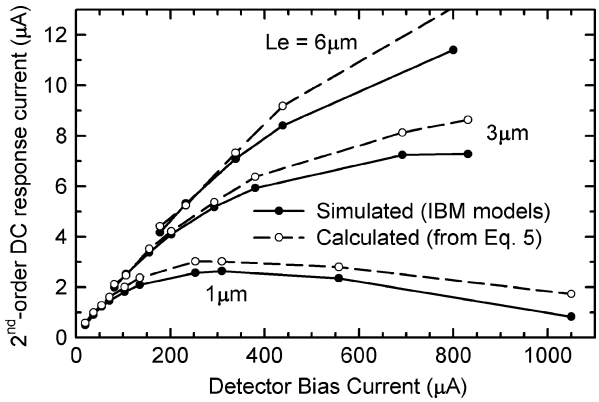

Fig. 3. Simulated and calculated (5) transistor second-order dc current response versus bias current for a 20-$\mathrm{mV_{pp}}$ 94-GHz input signal.

described in the Appendix, the second-order dc response is calculated using a Volterra series expansion, and is

$$I_{\mathrm{dc}} = \frac{{V_s}^2}{2V_t\left[(1+g_mR_e)^2 + R^2\omega^2\left(\frac{g_m}{\omega_t}+C_{je}\right)^2\right]} \times \frac{g_m}{1+g_mR_e} \tag{5}$$

where $R = R_b + R_e$, R_b is the base resistance, R_e is the emitter resistance, and V_s is the applied voltage at the transistor base. This expression can be evaluated using parameters given in the process documentation without the need of a SPICE or Volterra solver.

Fig. 3 compares the simulated (Cadence, IBM transistor models) and calculated dc response current with a 94-GHz input signal (20 $\mathrm{mV_{pp}}$). Equation (5) was evaluated using estimated values of r_b, r_e, C_{je}, and ω_t provided in the *IBM 8HP Design Manual*. Fig. 3 shows that the slope of the second-order response versus bias current, $\partial\Re/\partial I$, decreases as bias current increases. For the detector circuit shown in Fig. 2, the low-frequency noise above the $1/f$ corner frequency is dominated by the multiplication of the bias network noise by g_mR_L. This is proportional to bias current, and is largely independent of transistor size. Therefore, the minimum NEP is obtained when the transistor is biased in the region where $\partial\Re/\partial I$ is maximized [see Fig. 4(a)], and this occurs with the smallest transistor size and lowest bias currents. However, smaller transistors exhibit increased $1/f$ noise [see Fig. 4(b)] and require increased matching network complexity to provide 50-Ω matching and large bandwidth. The final choice of transistor size is, therefore, determined by a tradeoff among minimum NEP, allowable $1/f$ noise corner, and the loss/bandwidth/complexity of the

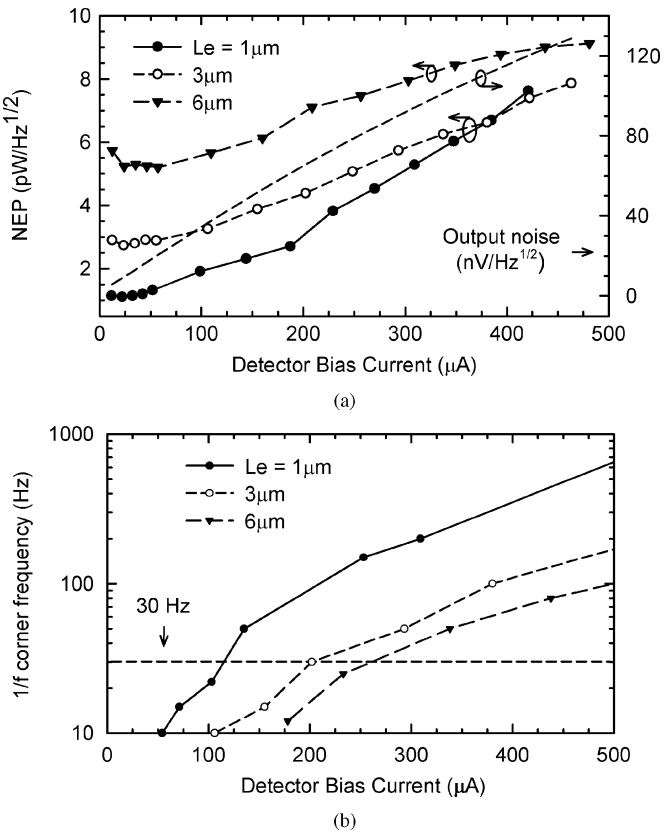

Fig. 4. Simulated: (a) output noise and NEP (neglecting $1/f$ noise) for the detector circuit shown in Fig. 2 using a 5-kΩ bias resistor and 750-Ω load resistor. (b) Transistor $1/f$ noise corner frequency versus bias current.

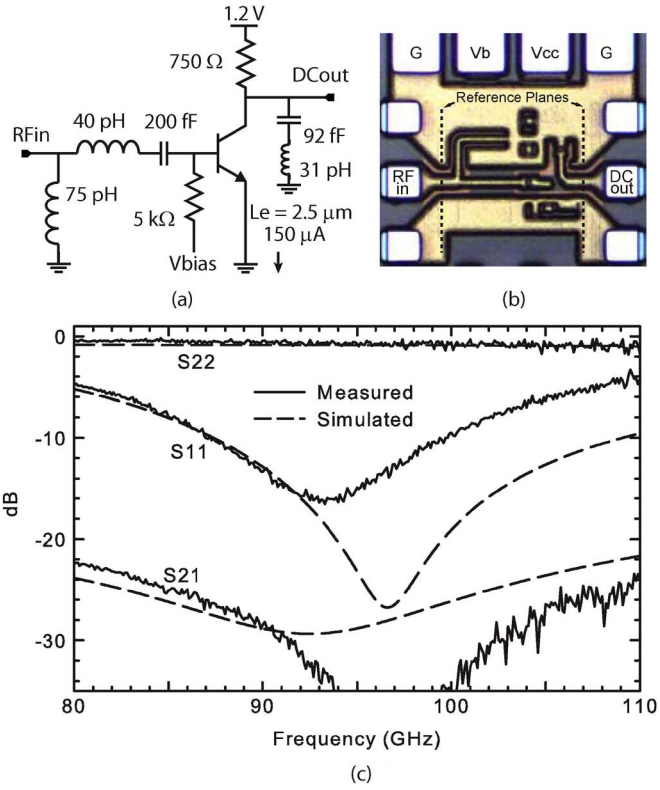

Fig. 5. (a) Detector schematic, (b) chip micrograph ($386 \times 370\ \mu\text{m}^2$ including pads), and (c) measured S-parameters. S_{12} is < -30 dB and is not shown.

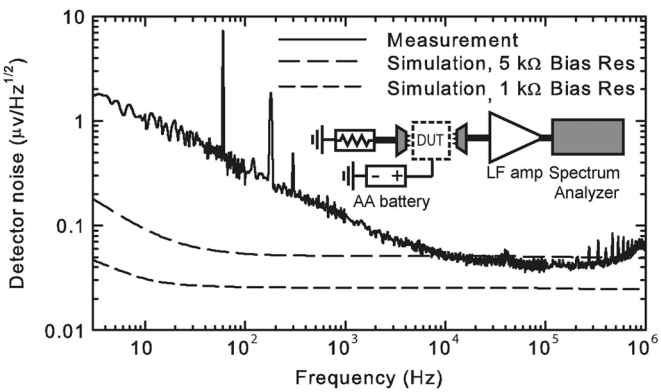

Fig. 6. Measured and simulated detector $1/f$ noise with noise test setup, 150-μA bias current.

matching network. A transistor emitter length of 2.5 μm was chosen with a bias current of 150 μA for our detector to achieve near-minimum NEP with sufficiently low $1/f$ noise and a simple 50-Ω input matching network.

The schematic, layout, and measured S-parameters for an on-chip W-band detector are shown in Fig. 5. The output 94-GHz notch filter is implemented using an IBM design-kit metal–insulator–metal (MIM) capacitor and short series transmission line, and a large output resistor (750 Ω) is used to achieve a high dc responsivity. The detector occupies 0.14 mm^2 including pads, and is biased using a simple current mirror.

The measured detector S-parameters agree well with simulations, having a W-band input match, and the notch filter response is clearly visible in S_{21} [see Fig. 5(c)]. On-chip thru-reflect-line (TRL) structures were used to define the reference planes, as shown Fig. 5(b). The detector noise was measured using a 50-Ω waveguide termination at the RF input port and with battery biasing and includes the external low-frequency amplifier noise (SRS 552 [23]) (seeFig. 6). The SRS amplifier has an input impedance of 100 kΩ and a noise figure of 1 dB (1.9 nV/$\sqrt{\text{Hz}}$) when driven by a 1-kΩ source, which is negligible compared to the detector noise (>40 nV/$\sqrt{\text{Hz}}$). The measured noise also increases above 500 kHz due to the external low-frequency amplifier.

The measured $1/f$ noise is higher than anticipated due to noise from the bias and load polysilicon resistors [see Fig. 5(a)], which is not modeled in the IBM design kit. For SiGe polysilicon resistors, the $1/f$ component of the voltage noise power spectral density S_e (in volts square per hertz) can be described by

$$S_e = \frac{C}{\text{WLf}^{\gamma}} V^2 \tag{6}$$

where W and L are the resistor width and length in micrometers, and C and γ are process-specific constants ($\gamma \approx 0.861$) [24]. To achieve a compact layout and small parasitic capacitances, the minimum allowable physical dimensions were used in the layout, which maximized the $1/f$ noise of the polysilicon resistors. In future designs, significant reductions in the $1/f$ noise would be possible using physically larger resistors. The detector

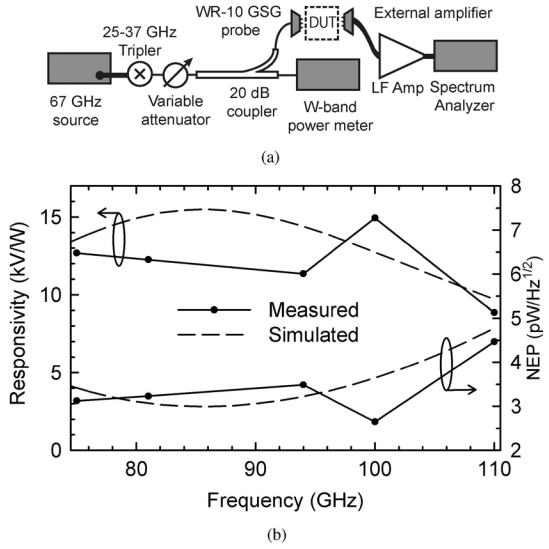

Fig. 7. (a) Test setup for responsivity measurements. (b) Detector responsivity and NEP, $P_{\rm in} = -42$ dBm. The detector bias current is 150 μA.

noise above the $1/f$ corner can also be reduced by using lower value bias resistors in the bias network (Fig. 6) or using an *LC* bias choke.

The detector responsivity was measured using a W-band tripler and the external LNA [see Fig. 7(a)]. The input RF signal was square-wave modulated at 10–100 kHz so as to be above the $1/f$ corner frequency. The output spectrum (signal and noise) was measured using an Agilent spectrum analyzer (E4448C), and the external amplifier gain was normalized out of the measurement [see Fig. 7(b)]. The detector achieves a measured NEP of 3–4 pW/$\sqrt{\rm Hz}$ with a responsivity of 12 ± 3 kV/W over the W-band range. The simulated input $\rm P_{1dB}$ is -15 dBm. Fig. 8 shows the measured responsivity, output noise, and NEP at 94 GHz. For low bias currents, the output noise (above the $1/f$ corner frequency) and responsivity increase linearly with bias current, and the NEP is nearly constant (less than 7% variation from 25 to 150 μA). The detector can be operated anywhere in the 25–150-μA region, but the current of 150 μA results in near-minimum NEP with a factor of 6 higher responsivity than the 25-μA bias current—this extra responsivity reduces the effect of environmental noise contributions in testing. Neglecting the $1/f$ noise contribution and using (4) with $B = 20$ GHz and $\tau = 30$ ms, we find $\Delta T_M \approx 45$ K, indicating that preamplification is necessary to achieve <0.5-K temperature resolution.

C. W-Band LNA

Neglecting LNA gain variations and the $1/f$ noise, the composite ΔT_M for a total-power radiometer with preamplification is given by

$$\Delta T_M = \sqrt{\left[2{T_S}^2 + \left(\frac{v_n}{\Re kG}\right)^2 \frac{1}{B}\right]\frac{B_{\rm LF}}{B}} = \sqrt{\left[\frac{2{T_S}^2}{B} + \left(\frac{\rm NEP}{kGB}\right)^2\right]\frac{1}{2\tau}} \quad (7)$$

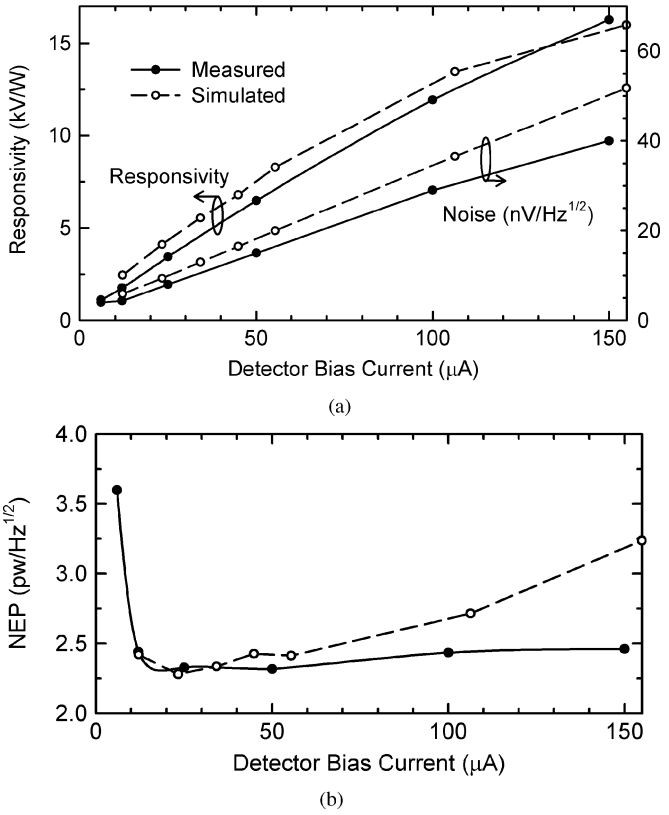

Fig. 8. (a) Measured and simulated detector noise (above 10 kHz) and responsivity. (b) Resulting NEP versus bias current. Measurements done at 94 GHz, $P_{\rm in} = -42$ dBm.

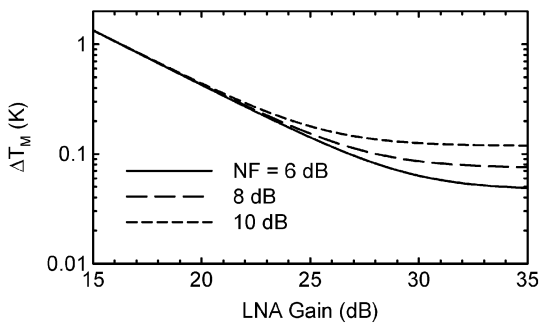

Fig. 9. Calculated minimum temperature resolution [ΔT_M, (7)] for a preamplified total-power radiometer using the detector in Section II-B with $B = 20$ GHz and $\tau = 30$ ms.

where $B_{\rm LF}$ is the output bandwidth, T_S is the system noise temperature, as shown in Fig. 1,, and G is the LNA gain [3], [25]. For an ideal integrator with integration time τ, the equivalent noise bandwidth $B_{\rm LF} = 1/(2\tau)$ [14], and (7) reduces to (2) for a high-gain LNA and to (4) for the case of no preamplification. Fig. 9 shows the achievable ΔT_M using the developed SiGe detector in (NEP = 3–4 pW/$\sqrt{\rm Hz}$ above 10 kHz) versus LNA gain and noise figure. Temperature resolutions of 0.1–0.5 K are achievable for a total-power radiometer with an LNA gain of 20–28 dB, depending on the LNA noise figure.

For the total-power radiometer, a five-stage LNA was designed using the procedure presented in [15]. The bias currents are chosen for low noise in stages 1 and 2 and for high gain in stages 3–5 (see Fig. 10). The input transistor is sized to provide

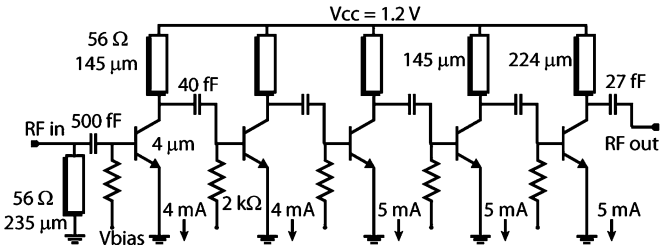

Fig. 10. LNA schematic. Interstage MOM caps are made between metal layers M3 and M4 in the interconnect stackup.

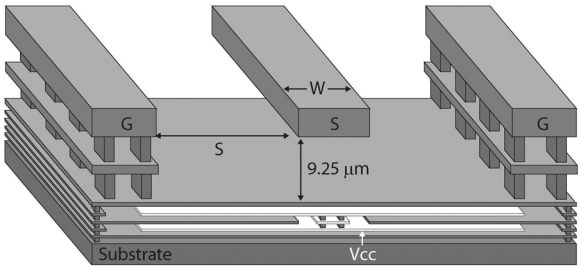

Fig. 11. Transmission lines in the IBM 8HP stackup. Five-layer MOM decoupling capacitors are built below the transmission lines.

simple matching with near-minimum noise figure. Shunt transmission line stubs and small metal–oxide–metal (MOM) capacitors provide interstage matching (see Fig. 11). Each stage uses five-layer MOM capacitors beneath the inductive transmission line loads to provide approximately 5 pF of total supply decoupling capacitance at W-band. The 56-Ω transmission line stubs have a signal width $W = 11$ μm and spacing $S = 11$ μm, and have Q's of 9–15 from 80 to 100 GHz (including via resistances for connections to transistors). Deep trench is placed beneath the interstage matching capacitors to reduce substrate coupling.

Fabricated LNAs were received from two separate wafer runs; the layout is shown in Fig. 12(a). The first LNA, which we refer to as LNA 1 and was presented in [10], achieves a peak gain of 23 dB [see Fig. 12(b)], and matches simulations closely. The simulated noise figure of this LNA is ≈8 dB and was not measured; the noise figure of a similar LNA was measured in [15] and agreed well with simulations. The LNAs from the second run, referred to as LNA 2, exhibit higher gain than anticipated, with a peak gain of 27 dB and >24-dB gain from 82 to 100 GHz. The additional gain can partially be explained if a "fast" wafer was received from the foundry—the S_{21} simulation associated with LNA 2 shown in Fig. 12(b) is the result of using the "fast" n-p-n process corners provided by IBM. S_{11}, S_{12}, and S_{22} are similar for both LNAs, and the LNAs are unconditionally stable; $K > 1$ and $|\Delta| < 1$ from dc–110 GHz with $K \approx 1.85$ and $|\Delta| \approx 0.10.4$ at W-band for the high-gain LNA. The source of this additional gain in the second LNA run remains under investigation; no low-frequency oscillations have been observed, and as mentioned, the LNA is unconditionally stable.

D. Total-Power Radiometer: Results

A total-power radiometer, constructed using the 23-dB gain W-band LNA (LNA 1) and power detector [see Fig. 13(a)], was fabricated and characterized. Responsivity was measured

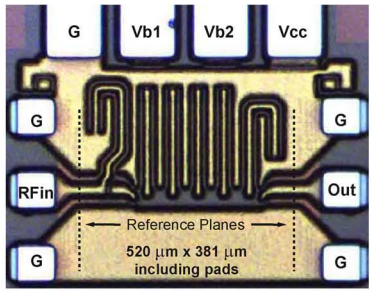

(a)

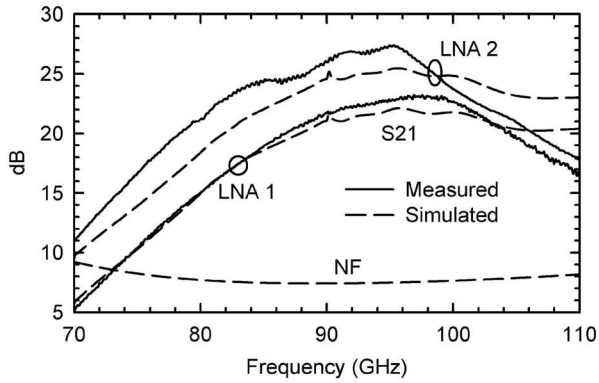

(b)

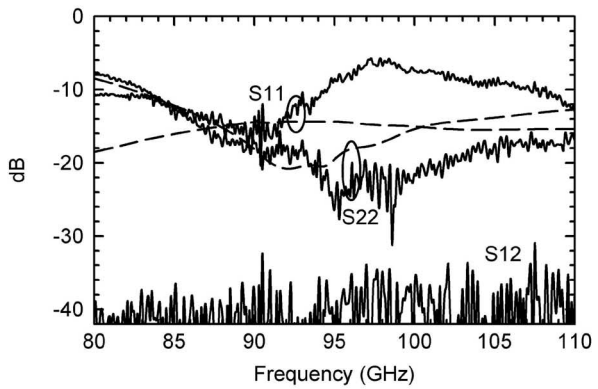

(c)

Fig. 12. (a) W-band LNA chip micrograph. (b) Measured LNA gain (simulated noise figure) for both LNA 1 and LNA 2. (c) Measured LNA S-parameters (shown for LNA 2, both are similar). The simulation line in (b) associated with LNA 2 utilizes a "fast" foundry process corner.

using a setup similar to that shown in Fig. 7, with an additional 20-dB coupler to prevent saturation of the amplifier or detector. The measured LNA + detector chip shows a responsivity of 4 ± 0.4 MV/W at 90–94 GHz and a 3-dB bandwidth of ∼83–103 GHz, with the detector biased at the 150-μA design current [see Fig. 13(b)]. The measured LNA + detector chip input 1-dB compression is roughly −38 dBm at 94 GHz, which is high enough for radiometer applications and is limited by the detector $P_{1\text{dB}}$ (-15 dBm $-23 = -38$ dBm), see Fig. 14. The measured output noise is 70 nV/$\sqrt{\text{Hz}}$, roughly 2× larger than the stand-alone detector noise [seeFig. 13(c)]. Again, the $1/f$ noise contribution from the polysilicon bias resistors in the LNA and in the detector is clearly seen. The NEP, calculated from the measured data at 90–104 GHz and assuming a noise of 70 nV/ $\sqrt{\text{Hz}}$, is shown in Fig. 13(d). An agreement between simulation and measurement is observed because both the LNA

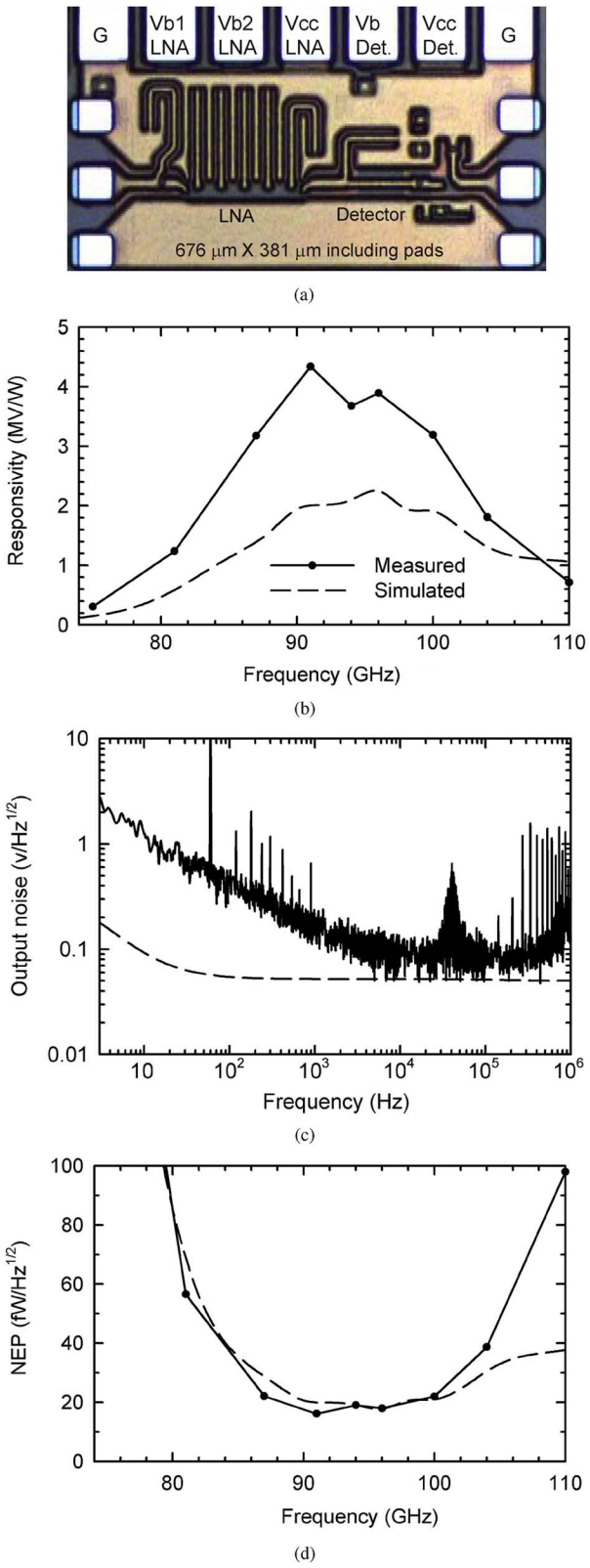

Fig. 13. Fabricated LNA + detector: (a) chip micrograph, (b) measured responsivity, (c) measured $1/f$ noise, and (d) NEP (using noise at 10 kHz).

gain and measured noise are higher than that simulated. The NEP can be improved to 13–14 fW/$\sqrt{\text{Hz}}$ if the detector operating current is reduced to 25–50 μA, as shown in Fig. 15.

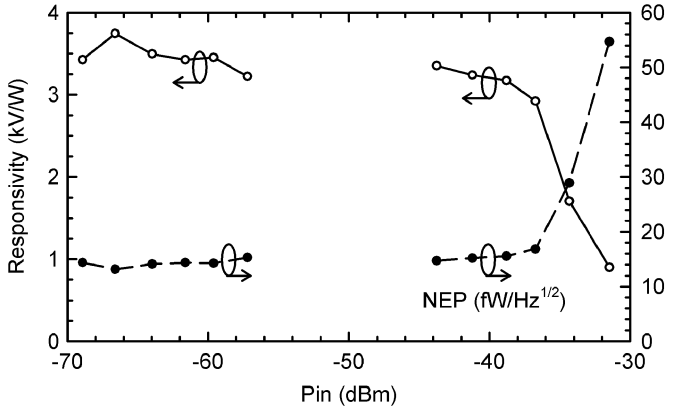

Fig. 14. Measured LNA + detector responsivity (and calculated NEP) versus input power at 94 GHz. The detector bias current is 150 μA.

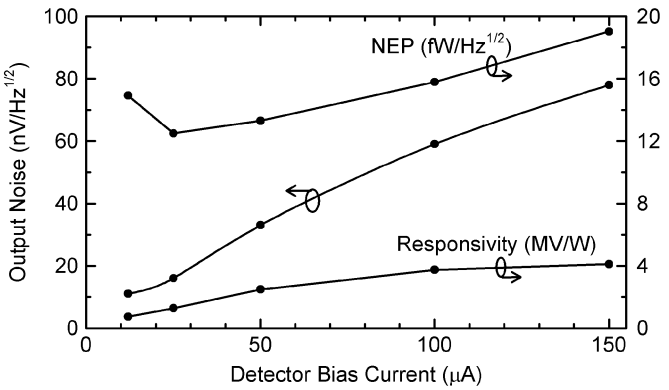

Fig. 15. Measured LNA + detector noise (above 10 kHz), responsivity, and resulting NEP versus bias current. Measurements done at 94 GHz with $P_{\text{in}} = -64$ dBm.

From (4), the total system $\Delta T_M \approx 0.34$ K, using the average NEP over the 3-dB bandwidth. The presence $1/f$ noise and LNA gain variations, however, necessitates periodic calibration or electrical/mechanical chopping, thus increasing the effective ΔT_M to $2 \cdot 0.34$ K $= 0.69$ K. Mechanical calibration/chopping is typically limited to a maximum frequency of several hundred hertz. This radiometer would therefore require a chopping frequency of $\geq$10 kHz, which can be accomplished using an integrated CMOS SPDT switch.

III. Dicke Radiometer

A. System Topology

The $1/f$ noise of the total-power radiometer can be overcome by electronic chopping above the $1/f$ corner frequency, as shown in Fig. 16, with a factor of 2 penalty in temperature resolution. Therefore, a W-band RF power detector, LNA, and SPDT switch are implemented in SiGe, followed by external amplification. The input W-band SPDT is alternately switched to the antenna or reference resistor, and output Dicke switching and integration is accomplished using digital processing.

B. W-Band SPDT Switch

Fig. 17(a) presents a $\lambda/4$ shunt-tuned CMOS SPDT switch and equivalent-circuit representation with gate bias voltages ap-

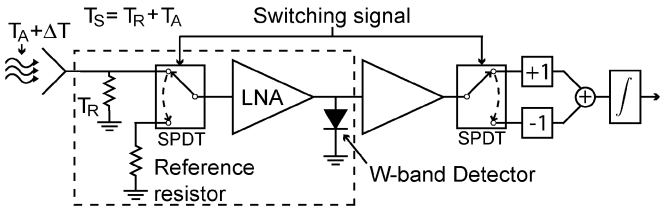

Fig. 16. Proposed SiGe Dicke-switched radiometer. The input SPDT, reference resistor, LNA, and W-band detector are integrated in a single chip.

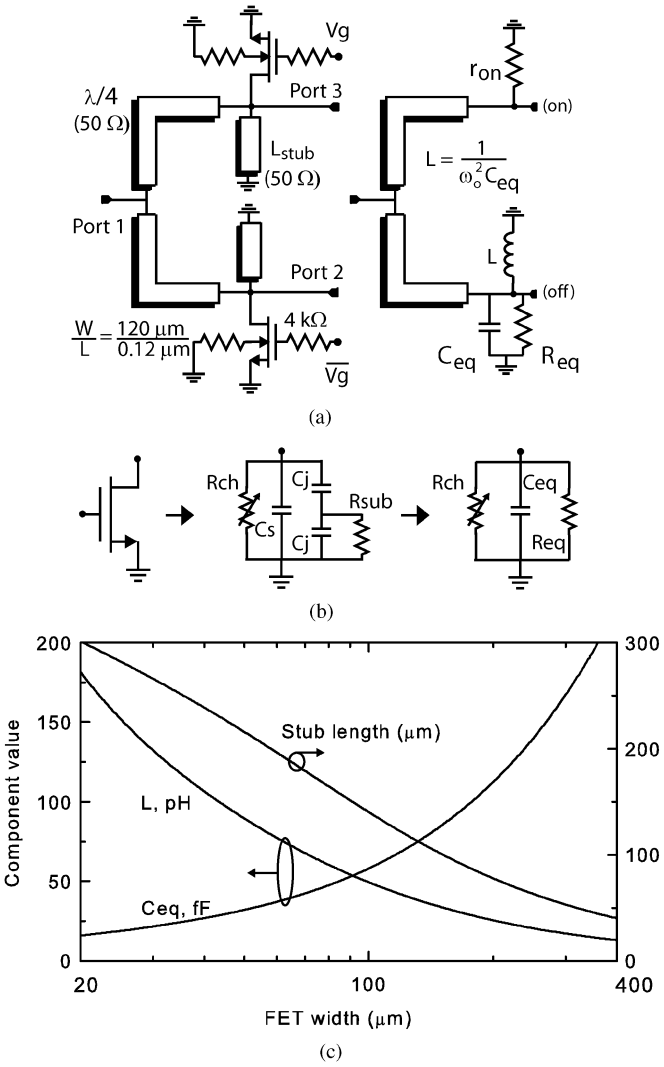

Fig. 17. (a) Circuit schematic for shunt-tuned $\lambda/4$ SPDT switch with simplified schematic for port 3 FET biased in the on-state (isolation). (b) FET equivalent-circuit model. (c) Tuning inductance, stub length, and $C_{\rm eq}$ versus FET width at 94 GHz.

plied (1.2 or 0 V). The shunt-FET SPDT topology has been previously demonstrated at W-band using 100-nm InAlGaAs HEMTs in [26]. As described in [27], the transistor junction, gate capacitances, and substrate resistance form an equivalent capacitance $C_{\rm eq}$ and resistance $R_{\rm eq}$ [see Fig. 17(b)]. A shunt inductor $L_{\rm stub} = 1/(\omega_o^2 C_{\rm eq})$ results in a parallel resonant circuit with the equivalent capacitance $C_{\rm eq}$ and an open circuit for the through port [Port 2 in Fig. 17(a)]. This inductance is synthesized using shorted transmission line stubs ($l_{\rm stub} = 105$ μm at 94 GHz for an FET width of 120 μm) with Q $\approx$ 25 at

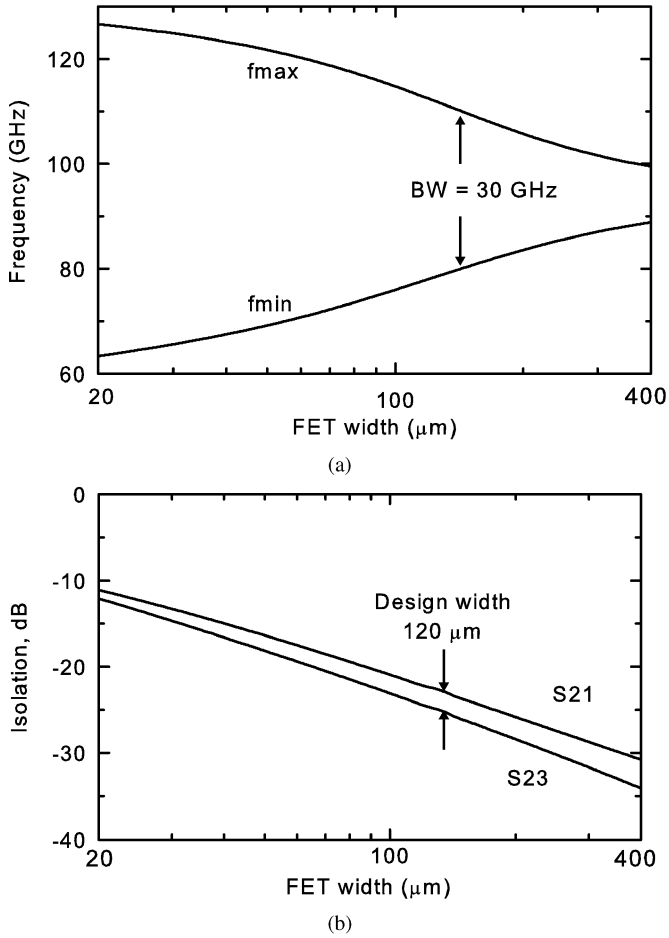

Fig. 18. Simulated: (a) -10-dB return loss matching BW and (b) isolation versus transistor width at 94 GHz.

90–100 GHz. The isolation port [Port 3 in Fig. 17(a)] is achieved using a shunt resistance to ground $(r_{\rm on})$, and quarter-wave lines are used in order to synthesize an open circuit at the common port of the SPDT switch ($\lambda/4$ section: $l = 385$ μm at 94 GHz). A triple-well floating-body design is used to increase power handling [28]; the FET body terminal is tied to ground through a large bias resistor and the n-well is tied to the Vcc. The FETs are separated by deep trench to increase isolation.

The simulated $C_{\rm eq}$ and resulting inductance values and stub lengths for varying FET widths are shown in Fig. 17(c), which determine the matching bandwidth. The -10-dB return-loss minimum and maximum frequencies with ideal transmission lines and tuning inductors are presented in Fig. 18 (the 3-dB insertion loss bandwidth is much greater than the impedance matching bandwidth, so the matching bandwidth is used in the design). The available isolation for each transistor width is also presented in Fig. 18. An FET width of 120 μm was chosen in order to allow matching from 80 to 110 GHz and results in an isolation of 21 dB at 94 GHz.

The fabricated SPDT switch and measured S-parameters are shown in Fig. 19. One port was terminated with an on-chip 50-Ω resistor to facilitate S-parameter measurements. The switch achieves 2.3-dB insertion loss with 21-dB isolation, and is well matched from 85 to 105 GHz. This performance is comparable to the W-band InAlGaAs high electron-mobility transistor (HEMT) SPDT described in [26], but is implemented

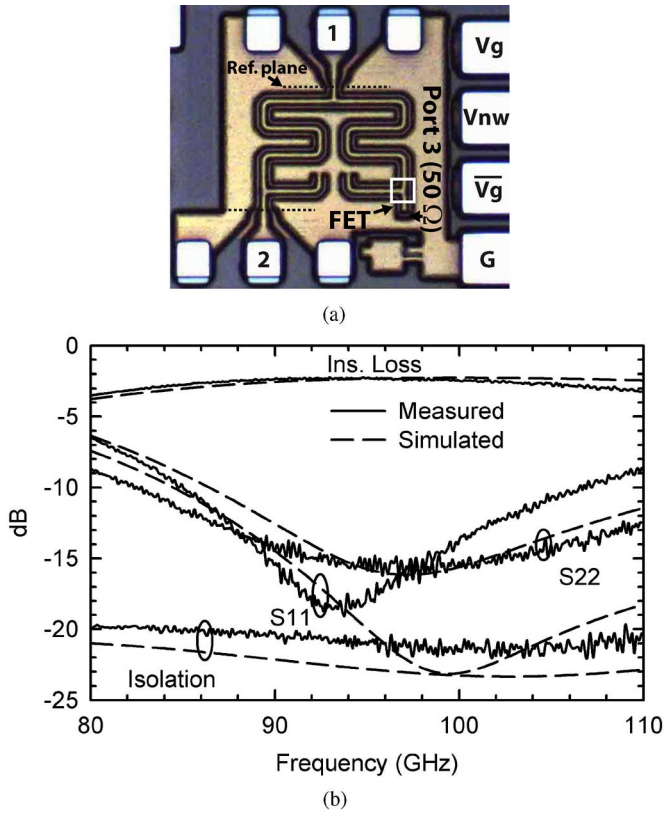

Fig. 19. (a) Fabricated SPDT switch. The chip is $370 \times 480\ \mu\text{m}^2$ with pads and $190 \times 250\ \mu\text{m}^2$ without pads. (b) Measured SPDT S-parameters.

TABLE I
SPDT PERFORMANCE COMPARISON

Ref, year	Freq. (GHz)	I.L. (dB)	Isol. (dB)	Size (mm^2)	Tech.
This work	**85-105**	**2.3**	**21**	**0.18**	**0.12μm (Bi)CMOS**
[29], 2009	60-94+	4.0	26	0.06	65 nm CMOS
[30], 2007	50-94	2.7	29	0.24	90 nm CMOS
[31], 2006	60-135	5.5	42	0.68	0.15μm GaAs HEMT
[32], 2003	30-85	2.5	33	1.45	0.15μm GaAs HEMT
[26], 2008	70-120	1.5	20	0.70	0.10μm InAlGaAs

in a smaller area (0.19 mm^2 versus 0.75 mm^2). Table I summarizes the SPDT performance in comparison with other W-band SPDT switches.

C. Dicke Radiometer Results

The W-band passive imaging chip integrating a W-band SPDT switch, W-band LNA, and power detector was fabricated in the IBM SiGe BiCMOS 8HP process and occupies $0.86 \times 0.46\ \text{mm}^2$ including pads [see Fig. 20(a)]. The switched radiometer chip includes the high-gain LNA (LNA 2) described in Section II-C. Measured S_{21} is shown with the SPDT switched both to the reference load and the input port, and the expected 20-dB difference is observed [see Fig. 20(b)]. The switching functionality was also verified using two phase-locked Agilent E33220A signal sources to drive the SPDT bias pins at 1–10 kHz with a continuous 94-GHz input signal. The chip has 80 nV/$\sqrt{\text{Hz}}$ output noise at 10 kHz, a responsivity $>$2.5 MV/W from 85–99 GHz, and a corresponding average NEP of 21 fW/$\sqrt{\text{Hz}}$ (Fig. 21). This imaging chip can achieve

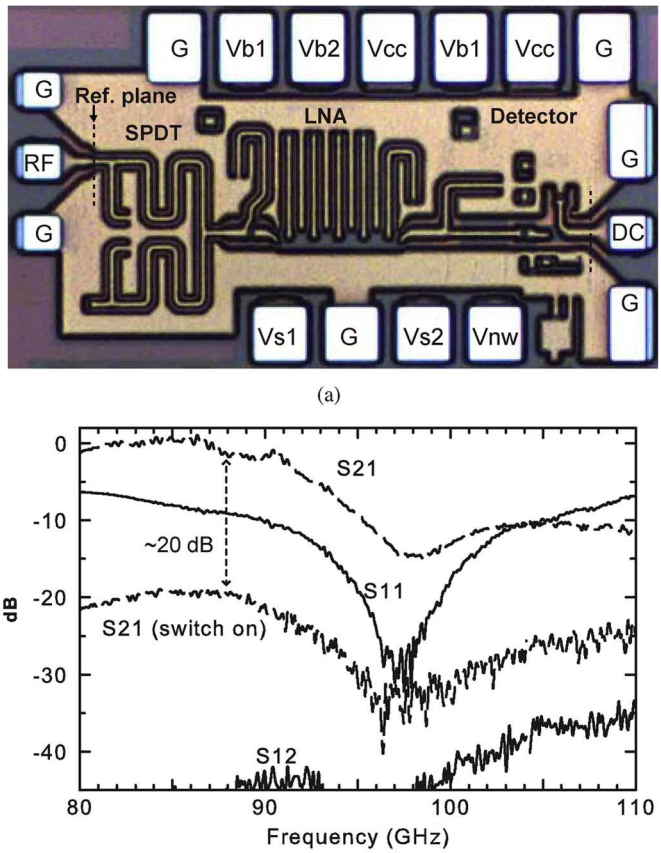

Fig. 20. (a) Switched-radiometer chip micrograph, $860 \times 460\ \mu\text{m}^2$ including pads. (b) Measured S-parameters. Note the 94-GHz notch filter response in S_{21}.

$\Delta T_M = 0.83$ K (using (4) and with a factor of 2 penalty for Dicke switching) when used as part of a focal-plane array with a video-rate 30-ms integration time (ΔT_M will increase if used as part of a column- or raster-scanned video-rate imager having reduced pixel integration time). The measured responsivity and output noise are higher than anticipated due to the increased LNA gain. The receiver performance is summarized in Table II.

IV. CONCLUSION

A W-band power detector, LNA, and SPDT were developed in a commercial 0.12-μm SiGe BiCMOS process, and integrated to implement a compact 94-GHz switched Dicke radiometer. The minimum temperature sensitivity of this system, 0.83 K, is comparable to that of recently reported radiometer modules (see Table III). This is, to our knowledge, the first W-band radiometer module implemented in SiGe or CMOS with state-of-the-art temperature sensitivity. Changes in the detector and LNA bias networks should result in reduced $1/f$ and broadband noise, and this combined with increasing the LNA gain to 30 dB can improve temperature sensitivity to $<$0.2 K. In fact, a low $1/f$ noise W-band detector was recently demonstrated using large-area bias resistors in the Jazz SBC18H2 process [33]. In the near future, it will also be possible to build such a system using advanced CMOS nodes, perhaps with a penalty in output noise and NEP [29].

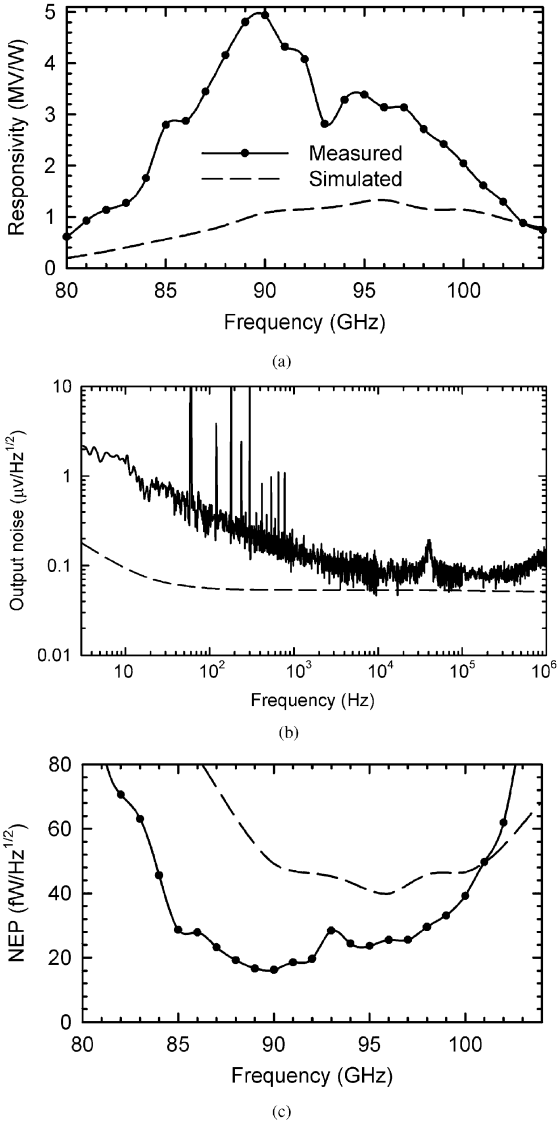

Fig. 21. Measured and simulated switched-radiometer: (a) responsivity, (b) output noise (above 10 kHz), and (c) and resulting NEP versus frequency. Measurements done at $P_{\rm in} = -64$ dBm.

TABLE II
W-BAND SWITCHED RADIOMETER SUMMARY

Responsivity	2.5-5 MV/W
Output noise	80 nV/$\sqrt{\text{Hz}}$
NEP (@ 10 kHz)	21 fW/$\sqrt{\text{Hz}}$
BW	85-99 GHz
ΔT_M ($\tau = 30$ ms)	0.83 K
Voltage	1.2V
Current	29 mA
Size	860 μm $\times$ 460 μm = 0.40 mm^2

APPENDIX
DERIVATION OF SQUARE-LAW DC RESPONSE

Using the large-signal HBT model shown in Fig. 2, the collector current can be described by a Volterra series expression

$$I_c = A_1(s) \circ V_s + A_2(s_1, s_2) \circ {V_s}^2 + A_3(s_1, s_2, s_3) \circ {V_s}^3 + \cdots \quad (8)$$

TABLE III
W-BAND RADIOMETER COMPARISON[1]

Ref, year	NEDT[2] (K)	Freq. (GHz)	Technology
This work	**0.69**	**83-103**	**SiGe LNA+Detector**[3]
This work	**0.83**	**84-99**	**SiGe SPDT+LNA+Detector**
[5], 2008	0.14	80-100	InP LNA, AlSb-heterostruct diode
[8], 2007	0.32	94$\pm$3	InAlGaAs LNA+Mixer MMIC
[7], 2008	2.3	75-135	Sb-heterostructure diode in WR-10 waveguide
[6], 2008	2.47	90-110+	InGaAs/InP diode array with integrated antenna

[1] First four entries use preamplification.
[2] Assumes 30 ms integration time; for 'This work' calculated with measured NEP (Eq. 4), other entries are measured NEDTs.
[3] A factor of 2 was included for external switching.

for an applied base voltage V_s, where the $\circ$ operator indicates adjusting ${V_s}^n$ by the magnitude and phase of the Volterra series kernel $A_n()$ at a given frequency. The dc response is described primarily by the $A_2()$ term with $s_1 = -s_2$. The third-order term does not contribute to output dc components, and higher order terms can be neglected for sufficiently small input signals.

The first two Volterra kernels for a common-emitter HBT with arbitrary base and emitter impedances Z_b and Z_e are derived in [22], and are shown as follows:

$$A_1(s) = \frac{g_m}{sC_{je}Z(s) + s\tau_F g_m Z(s) + \frac{g_m Z(s)}{\beta_0} + 1 + g_m Ze(s)} \quad (9)$$

$$A_2(s_1, s_2) = A_1(s_1 + s_2)A_1(s_1)A_1(s_2)\frac{V_T}{2{I_Q}^2} \times [1 + (s_1 + s_2)C_{je}Z(s_1 + s_2)]. \quad (10)$$

To examine the dc response for an input at frequency w, we set $s_1 = -s_2 = s$ and find

$$A_2(s, -s) = A_1(0)A_1(s)A_1(-s)\frac{V_T}{2{I_Q}^2}. \quad (11)$$

Neglecting the finite low-frequency current gain β_0 and setting $\tau_F = 1/\omega_t$ yields (12) as follows:

$$A_2(s, -s) = \frac{1}{2V_t\left[(1 + g_m Z_e(s))^2 + Z(s)^2\omega^2\left(\frac{g_m}{\omega_t} + C_{je}\right)^2\right]} \times \frac{g_m}{1 + g_m R_e(0)}. \quad (12)$$

The second-order dc current response is then found by multiplying ${V_s}^2 \times A_2(s, -s)$, considering only the resistive base and emitter impedances results in (5) and is presented in Section II-B.

ACKNOWLEDGMENT

The authors would like to thank M. Chang, The University of Michigan at Ann Arbor, Dr. S. Weinreb, California Institute of Technology, Dr. H. Kazemi, HRL Laboratories, Malibu, CA, Dr. J. Lynch and Dr. H. Moyer, both with HRL Laboratories

LLC, Malibu, CA, Dr. T. Kenny, Defense Advanced Research Projects Agency (DARPA), Arlington, VA, and A. Hung, Army Research Laboratories, Adelphi, MD, for their help and fruitful discussions. The SiGe chips were fabricated using the Trusted Access Program Office, DARPA.

REFERENCES

[1] I. Jaeger, L. Zhang, J. Stiens, G. Koers, H. Sahli, and R. Vounckx, *W-Band Speckle Contrast Images for Inspection of Concealed Objects*, W. Osten, C. Gorecki, and E. L. Novak, Eds. Bellingham, WA: SPIE, 2007, vol. 6616, p. 66160Y. [Online]. Available: http://link.aip.org/link/?PSI/6616/66160Y/1

[2] S. Mollenkopf, L. P. B. Katehi, and G. M. Rebeiz, "A low-cost 20–22 GHz MIC active receiver/radiometer," *IEEE Trans. Microw. Theory Tech.*, vol. 43, no. 4, pp. 989–993, Apr. 1995.

[3] H. P. Moyer, J. J. Lynch, J. N. Schulman, R. L. Bowen, J. H. Schaffner, A. K. Kurdoghlian, and T. Y. Hsu, "A low noise chipset for passive millimeter wave imaging," in *IEEE MTT-S Int. Microw. Symp. Dig.*, Honolulu, HI, Jun. 2007, pp. 1363–1366.

[4] H. Kazemi, G. Nagy, L. Tran, E. Grossman, E. R. Brown, A. C. Gossard, G. D. Boreman, B. Lail, A. C. Young, and J. D. Zimmerman, "Ultra sensitive ErAs/InAlGaAs direct detectors for millimeter wave and THz imaging applications," in *IEEE MTT-S Int. Microw. Symp. Dig.*, Honolulu, HI, Jun. 2007, pp. 1367–1370.

[5] J. J. Lynch, H. P. Moyer, J. H. Schaffner, Y. Royter, M. Sokolich, B. Hughes, Y. J. Yoon, and J. N. Schulman, "Passive millimeterwave imaging module with preamplified zero-bias detection," *IEEE Trans. Microw. Theory Tech.*, vol. 56, no. 7, pp. 1592–1600, Jul. 2008.

[6] H. Kazemi, C. Nguyen, B. Brar, G. Rebeiz, G. Nagy, L. Tran, A. Young, and E. R. Brown, "Low cost modular integrated horn antenna array using heterojunction barrier diode detectors," in *IEEE MTT-S Int. Microw. Symp. Dig.*, Atlanta, GA, Jun. 2008, pp. 297–300.

[7] J. H. Schaffner, J. J. Lynch, K. V. Guinn, J. N. Schulman, H. P. Moyer, R. Bowen, and M. Musni, *A Wideband Radiometer Module for an Unamplified Direct Detection Scalable W-Band Imaging Array*, R. Appleby and D. A. Wikner, Eds. Bellingham, WA: SPIE, 2008, vol. 6948, p. 694807. [Online]. Available: http://link.aip.org/link/?PSI/6948/694807/1

[8] D. Notel, J. Huck, S. Neubert, S. Wirtz, and A. Tessmann, "A compact mmw imaging radiometer for concealed weapon detection," in *Proc. Int. Terahertz Electron., Infrared Millimeter Waves Conf.*, Sep. 2007, pp. 269–270.

[9] L. Li, J. Yang, J. Xiong, J. Wu, Z. Jiang, and X. Zheng, "W-band Dicke-radiometer for imaging," *Int. J. Infrared Millim. Waves*, vol. 29, no. 9, pp. 879–888, 2008.

[10] J. W. May and G. M. Rebeiz, "High-performance W-band SiGe RFICs for passive millimeter-wave imaging," in *Proc. IEEE Radio Freq. Integr. Circuits Symp.*, Boston, MA, Jun. 2009, pp. 437–440.

[11] S. Weinreb, R. Lai, N. Erickson, T. Gaier, and J. Wielgus, "W-band InP wideband MMIC LNA with 30 K noise temperature," in *IEEE MTT-S Int. Microw. Symp. Dig.*, Anaheim, CA, 1999, vol. 1, pp. 101–104.

[12] F. Ulaby, R. Moore, and A. Fung, "Microwave remote sensing fundamentals and radiometry," in *Microwave Remote Sensing: Active and Passive*. Norwood, MA: Artech House, 1991.

[13] M. S. Hersman and G. A. Poe, "Sensitivity of the total power radiometer with periodic absolute calibration," *IEEE Trans. Microw. Theory Tech.*, vol. MTT-29, no. 1, pp. 32–40, Jan. 1981.

[14] M. Tiuri, "Radio astronomy receivers," *IEEE Trans. Antennas Propag.*, vol. AP-12, no. 7, pp. 930–938, Dec. 1964.

[15] J. W. May and G. M. Rebeiz, "A W-band SiGe 1.5 V LNA for imaging applications," in *Proc. IEEE Radio Freq. Integr. Circuits Symp.*, 2008, pp. 241–244.

[16] Y.-S. Jiang, Z.-M. Tsai, J.-H. Tsai, H.-T. Chen, and H. Wang, "A 86 to 108 GHz amplifier in 90 nm CMOS," *IEEE Microw. Wireless Compon. Lett.*, vol. 18, no. 2, pp. 124–126, Feb. 2008.

[17] J. Alvarado, K. T. Kornegay, B. P. Welch, and Y. W. Wang, "W-band SiGe LNA using unilateral gain peaking," in *IEEE MTT-S Int. Microw. Symp. Dig.*, Atlanta, GA, Jun. 2008, pp. 289–292.

[18] J. Kim and J. F. Buckwalter, "A DC–102 GHz broadband amplifier in 0.12 μm SiGe BiCMOS," in *Proc. IEEE Radio Freq. Integr. Circuits Symp.*, Boston, MA, Jun. 2009, pp. 53–56.

[19] J. N. Schulman, J. J. Lynch, H. P. Moyer, J. H. Schaffner, R. L. Bowen, Y. Royter, M. Sokolich, and R. D. Rajavel, *Unamplified Direct Detection W-Band Imaging Array*, R. Appleby and D. A. Wikner, Eds. Bellingham, WA: SPIE, 2007, vol. 6548, p. 65480F. [Online]. Available: http://link.aip.org/link/?PSI/6548/65480F/1

[20] S. Sankaran and K. K. O, "Schottky barrier diodes for millimeter wave detection in a foundry CMOS process," *IEEE Electron Device Lett.*, vol. 26, no. 7, pp. 492–494, Jul. 2005.

[21] R. M. Rassel, J. B. Johnson, B. A. Orner, S. K. Reynolds, M. E. Dahlstrom, J. S. Rascoe, A. J. Joseph, B. P. Gaucher, J. S. Dunn, and S. A. St. Onge, "Schottky barrier diodes for millimeter wave SiGe BiCMOS applications," in *Proc. Bipolar/BiCMOS Circuits Technol. Meeting*, Oct. 2006, pp. 1–4.

[22] K. L. Fong and R. G. Meyer, "High-frequency nonlinearity analysis of common-emitter and differential-pair transconductance stages," *IEEE J. Solid-State Circuits*, vol. 33, no. 4, pp. 548–555, Apr. 1998.

[23] *"Manual, Model SR550/552: Voltage Pre-Amplifier"* Stanford Res. Syst., , Sunnyvale, CA, 2001. [Online]. Available: http://www.thinksrs.com

[24] O. Roux dit Buisson and G. Morin, "Flicker noise characterization of polysilicon resistors in submicron BiCMOS technologies," in *Proc. IEEE Int. Conf. Microelectron. Test Struct.*, Monterey, CA, Mar. 1997, pp. 49–51.

[25] E. R. Brown, "Fundamentals of terrestrial millimeter-wave and THz remote sensing," *Int. J. High Speed Electron. Syst.*, vol. 13, pp. 995–1097, 2003.

[26] I. Kallfass, S. Diebold, H. Massler, S. Koch, M. Seelmann-Eggebert, and A. Leuther, "Multiple-throw millimeter-wave FET switches for frequencies from 60 up to 120 GHz," in *Proc. 38th Eur. Microw. Conf.*, Amsterdam, The Netherlands, Oct. 2008, pp. 1453–1456.

[27] B.-W. Min and G. M. Rebeiz, "Ka-band low-loss and high-isolation 0.13 μm CMOS SPST/SPDT switches using high substrate resistance," in *Proc. IEEE Radio Freq. Integr. Circuits Symp.*, Honolulu, HI, Jun. , pp. 569–572.

[28] M.-C. Yeh, Z.-M. Tsai, R.-C. Liu, K. Y. Lin, Y.-T. Chang, and H. Wang, "Design and analysis for a miniature CMOS SPDT switch using body floating technique to improve power performance," *IEEE Trans. Microw. Theory Tech.*, vol. 54, no. 1, pp. 31–39, Jan. 2006.

[29] A. Tomkins, P. Garcia, and S. P. Voinigescu, "A passive W-band imager in 65 nm bulk CMOS," in *Proc. IEEE Compound Semiconduct. Integr. Circuit Symp.*, Greensboro, NC, Oct. 2009, pp. 139–142.

[30] S. F. Chao, H. Wang, C. Y. Su, and J. G. J. Chern, "A 50 to 94-GHz CMOS SPDT switch using traveling-wave concept," *IEEE Microw. Wireless Compon. Lett.*, vol. 17, no. 2, pp. 130–132, Feb. 2007.

[31] Z.-M. Tsai, M.-C. Yeh, H.-Y. Chang, M.-F. Lei, K. Y. Lin, C.-S. Lin, and H. Wang, "FET-integrated CPW and the application in filter synthesis design method on traveling-wave switch above 100 GHz," *IEEE Trans. Microw. Theory Tech.*, vol. 54, no. 5, pp. 2090–2097, May 2006.

[32] J. Kim, W. Ko, S.-H. Kim, J. Jeong, and Y. Kwon, "A high-performance 40–85 GHz MMIC SPDT switch using FET-integrated transmission line structure," *IEEE Microw. Wireless Compon. Lett.*, vol. 13, no. 12, pp. 505–507, Dec. 2003.

[33] J. W. May, "SiGe integrated circuits for millimeter-wave imaging and phased arrays," Ph.D. dissertation, Elect. Comput. Eng. Dept., Univ. California at San Diego, La Jolla, CA, 2009.

Jason W. May (S'04–M'09) received the B.S. degree in electrical engineering from The University of Michigan at Ann Arbor, in 2004, and the M.S. and Ph.D. degrees in electrical engineering from the University of California at San Diego (UCSD), La Jolla, in 2007 and 2009.

While with UCSD, he was involved in Ka/Q- and W-band SiGe RFICs. In 2009, he joined HRL Laboratories, LLC, Malibu, CA, where he currently develops SiGe, CMOS, and III–V high-frequency circuits and systems.

Gabriel M. Rebeiz (S'86–M'88–SM'93–F'97) received the Ph.D. degree from the California Institute of Technology, Pasadena.

He is currently a Professor of electrical and computer engineering with the University of California at San Diego, La Jolla. From 1988 to 2004, he was with The University of Michigan at Ann Arbor, where he contributed to planar millimeter-wave and terahertz antennas and imaging arrays from 1988 to 1996, and where his group has optimized the dielectric-lens antennas, which is the most widely used antenna at millimeter-wave and terahertz frequencies. His group recently developed 6–18- and 30–50-GHz 8- and 16-element phased arrays on a single chip, making them one of the most complex RFICs at this frequency range. His group also demonstrated very high-Q RF microelectromechanical systems (MEMS) tunable filters from 4–6 GHz ($Q>300$) and the new angular-based RF MEMS capacitive and metal-contact switches. As a consultant, he developed the 24-GHz single-chip automotive radar with USM/ViaSat, X-, Ku-, and W-band phased arrays for defense applications, the RFMD RF MEMS switch, and the Agilent RF MEMS switch. He is the Director of the University of California at San Diego (UCSD)/Defense Advanced Research Projects Agency (DARPA) Center on RF MEMS Reliability and Design Fundamentals. He authored *RF MEMS: Theory, Design and Technology* (Wiley: 2003).

Prof. Rebeiz is the National Science Foundation Presidential Young Investigator. He has been an associate editor of the IEEE TRANSACTIONS ON MICROWAVE THEORY AND TECHNIQUES. He has been a Distinguished Lecturer for the IEEE Microwave Theory and Techniques Society (IEEE MTT-S) and the IEEE Antennas and Propagation Society. He was the recipient of the URSI Koga Gold Medal Recipient, the IEEE MTT-S Distinguished Young Engineer (2003), the 2000 IEEE MTT–S Microwave Prize, the 1998 Eta Kappa Nu Professor of the Year Award, the 1998 Amoco Teaching Award given to the best undergraduate teacher at The University of Michigan at Ann Arbor, and the 2008 Teacher of the Year Award of the Jacobs School of Engineering, UCSD.